Journal of Materials Chemistry C

Crystal Growth, Structural and Electronic Characterizations of Zero-Dimensional Metal Halide (TEP)$InBr_4$ Single Crystals for X-Ray Detection

Journal:	*Journal of Materials Chemistry C*
Manuscript ID	TC-ART-08-2023-002787.R1
Article Type:	Paper
Date Submitted by the Author:	02-Oct-2023
Complete List of Authors:	Zhang, Zheng; University of Oklahoma, Chemistry and Biochemistry Pugliano, Tony; University of Oklahoma, Department of Chemistry & Biochemistry Cao, Da; North Carolina State University at Raleigh Kim, Doup; North Carolina State University, Department of Nuclear Engineering Annam, Roshan Sameer; University of Oklahoma, Aerospace and Mechanical Engineering Popy, Dilruba; University of Oklahoma, Department of Chemistry & Biochemistry Pinky, Tamanna; University of Oklahoma, Chemistry and Biochemistry Yang, Ge; North Carolina State University, Department of Nuclear Engineering Garg, Jivtesh; University of Oklahoma, School of Aerospace and Mechanical Engineering Borunda, Mario; Oklahoma State University, Physics Saparov, Bayram; University of Oklahoma, Department of Chemistry & Biochemistry

Crystal Growth, Structural and Electronic Characterizations of Zero-Dimensional Metal Halide (TEP)$InBr_4$ Single Crystals for X-Ray Detection

Zheng Zhang[a], Tony M. Pugliano[a], Da Cao[b], Doup Kim[b], Roshan S. Annam[c], Dilruba A. Popy[a], Tamanna Pinky[a], Ge Yang[b], Jivtesh Garg[c], Mario F. Borunda[d], Bayram Saparov[a]*
[a]Department of Chemistry and Biochemistry, University of Oklahoma, Norman, OK 73019
[b]Department of Nuclear Engineering, North Carolina State University, Raleigh, NC 27607
[c]School of Aerospace and Mechanical Engineering, University of Oklahoma, Norman, OK 73019
[d]Department of Physics, Oklahoma State University, Stillwater, OK 74078

*Author to whom correspondence should be addressed: saparov@ou.edu

Abstract: Recently, metal halides have shown great potential for applications such as solar energy harvesting, light emission, and ionizing radiation detection. In this work, we report the preparation, structural, thermal, and electronic properties of a new zero-dimensional (0D) halide (TEP)$InBr_4$ (where TEP is tetraethylphosphonium organic cation, $C_8H_{20}P^+$). (TEP)$InBr_4$ single crystals are obtained within a few days of continuous crystal growth time via a solution growth methodology. (TEP)$InBr_4$ shows a relatively large optical bandgap energy of 4.32 eV and a low thermal conductivity between 0.33±0.05 and 0.45±0.07 W/m-K. Based on the density functional theory (DFT) calculations, the highest occupied molecular orbitals (HOMOs) of (TEP)$InBr_4$ are dominated by the Br states, while the lowest unoccupied molecular orbitals (LUMOs) are constituted by both In and Br states. (TEP)$InBr_4$ single crystals exhibit a semiconductor resistivity of 1.73×10^{13} Ω·cm and a mobility-lifetime (mu-tau) product of 2.07×10^{-5} cm^2/V. Finally, a prototype (TEP)$InBr_4$ single crystal-based X-ray detector with a detection sensitivity of 569.85 $uCGy^{-1}cm^{-2}$ (at electrical field E=100 V/mm) was fabricated, indicating the potential use of (TEP)$InBr_4$ for radiation detection applications.

1. Introduction

In the past decade, semiconductor materials such as cadmium zinc telluride (CZT) and gallium oxide Ga_2O_3 have been studied for X-ray and gamma-ray photon detection applications [1, 2]. Despite the success achieved so far, a few issues, such as high concentrations of Te inclusions and poor hole charge transport properties in CZT crystals [3, 4] have not been fully addressed. Recently, three-dimensional (3D) halide perovskites with the general chemical formula of ABX_3 (where A=Cs^+, MA^+, FA^+; B=Pb^{2+}; X=I^-, Br^-, Cl^-) and their structural derivatives have been investigated as promising alternatives for optoelectronic applications such as ionizing radiation detection, solid-state lighting and solar energy harvesting [5, 6, 7]. This new class of semiconducting materials possess outstanding characteristics including high charge carrier mobility, sufficiently long carrier lifetime, tunable bandgap energy, low density of trap states, and high detection sensitivity for X-ray photons, which enable their use in radiation detection [8, 9]. Moreover, metal halides can be obtained from room temperature wet chemistry reactions, leading to a much simpler and lower cost processing compared to the traditional melt growth methods used for CZT single crystals.

Among the investigated halide perovskite semiconductors for radiation detection applications, 3D materials such as methylammonium lead iodide ($MAPbI_3$) [9], formamidinium lead bromide

($FAPbBr_3$) [10], and cesium lead bromide ($CsPbBr_3$) [11] have shown promising performances. However, the toxicity of lead to the environment poses further development challenges for these 3D compounds [12, 13]. In the meantime, the polarization issue, a known phenomenon in halide-based semiconductors, including thallium bromide (TlBr) [14], also needs to be addressed appropriately. Lower-dimensional lead-free perovskite derivatives such as two-dimensional (2D) layered, one-dimensional (1D) chain and 0D cluster halides have greater chemical and structural tunability, which could offer ways to mitigate the polarization issue [15]. Among the broader metal halide family, few 0D metal halides have been investigated for semiconducting X-ray detection (e.g., $MA_3Bi_2I_9$ and $(DPA)_2BiI_9$) [16, 17], the inclusion of toxic Bi and I in these materials, however, requires further attention. It is thus of interest to explore other nontoxic 0D halides to fully reveal their potential for semiconductor radiation detector applications.

In this work, we report the synthesis, optical, thermal, and electronic properties of a new metal halide $(TEP)InBr_4$. The 0D crystal structure of $(TEP)InBr_4$ features isolated molecular TEP^+ cations and $[InBr_4]^-$ tetrahedral anions. Millimeter-sized single crystals of $(TEP)InBr_4$ can be obtained within a few days using a methanol (MeOH) solution growth method. The obtained crystals display relatively good air stability for at least a few days, which, however, show a crystallinity loss over weeks of air storage. Computational results for $(TEP)InBr_4$ indicate that it is a direct bandgap semiconductor. It has a relatively large bandgap energy of 4.32 eV as determined by optical spectroscopy experiments. To evaluate the X-ray response of this material, a prototype X-ray radiation detector using a $(TEP)InBr_4$ single crystal was fabricated; the detector showed a signal-to-noise ratio ~2860 to soft 8 keV X-rays with a detection sensitivity of 569.85 $uCGy^{-1}cm^{-2}$ (at electric field E=100 V/mm).

2. Experimental

2.1 Single crystal growth

Reactants tetraethylphosphonium bromide ($C_8H_{20}PBr$, TEPBr) and indium bromide ($InBr_3$) were purchased from commercial vendors TCI and Sigma-Aldrich, respectively, and were used as received. For $(TEP)InBr_4$ crystal growth, 0.5 mmol TEPBr and 0.5 mmol $InBr_3$ (molar ratio 1:1) were loaded into a 20 mL glass scintillation vial, then 8 mL methanol (MeOH) was added to dissolve the starting chemicals under continuous stirring at room temperature. The vial was then left uncapped at room temperature in open air for slow evaporation. After a few days of continuous growth time, mm-sized and colorless $(TEP)InBr_4$ single crystals can be harvested on the bottom of the vial. Crystal growth experiments were also carried out using different molar ratios of 2:1, 3:1, and 4:1, respectively (0.5 mmol, 0.75 mmol, 0.1 mmol respectively for TEPBr and 0.5 mmol $InBr_3$). All these reactions produced only $(TEP)InBr_4$, as confirmed by the measured powder X-ray diffraction data (see Fig. S1, Supporting Information (SI)). However, there were variations in the crystal quality and size depending on the loading ratios and evaporation rates. The best quality crystals from the stoichiometric reactions with 1:1 loading ratio were selected for property characterizations.

2.2 Single crystal and powder X-ray diffraction measurements

Single crystal X-ray diffraction (SCXRD) measurements were performed using a Bruker D8 Quest Kappa-geometry diffractometer with an Incoatec IμS microfocus Mo Kα X-ray source and a Photon II area detector. The structure was solved by intrinsic phasing methods (SHELXT) as embedded in the APEX3 v2015.5-2 program. Details of the single crystal data and structure refinement

parameters are in Table 1. Additional information can be obtained in the form of a CIF file, which can be found in the Cambridge Crystallographic Data Centre (CCDC) database (deposition number 2285870). For powder XRD measurements, a (TEP)$InBr_4$ single crystal was first powdered using a mortar pestle. The powder was then loaded to a Rigaku MiniFlex600 instrument equipped with Ni-filtered Cu Kα X-ray source. Powder XRD scans were performed using a step size of 0.02°.

2.3 Diffuse reflectance

Diffuse reflectance data were collected using a PerkinElmer Lambda 750 UV-Vis-NIR spectrometer equipped with a 100 mm Spectralon InGaAs Integrating Sphere detector. The data were transformed to Kubelka-Munk function F(R) using F(R) = $^{\alpha}/_{S} = (1-R)^2/2R$, where α is the absorption coefficient, S is the scattering coefficient, and R is the reflectance.

2.4 Differential scanning calorimetry (DSC)-thermogravimetric analysis (TGA)

DSC-TGA measurements were performed using TA Discovery SDT650 on ~6 mg (TEP)$InBr_4$ powder samples. The measurement was performed from 30 °C to 300 °C under inert nitrogen gas flow (flow rate of 100 mL/min) with a heating rate of 10 °C/min.

2.5 Device fabrication, electronic characterization, and X-ray radiation response testing

To measure the electrical properties and X-ray radiation response characteristics of (TEP)$InBr_4$, fast drying silver paste (purchased from Ted Pella, Inc.) was brushed onto two opposite sides of the selected single crystal samples. The crystal was then used for electronic measurements and X-ray response tests using the Keithley 6487 pico-ammeter. For mobility-lifetime (mu-tau) measurements, a mini-X2 tungsten X-ray tube (purchased from Amptek Inc.) was used as excitation source. For X-ray detection sensitivity measurement and response testing, the fabricated single crystal-based prototype detector was exposed to soft 8 keV X-rays, which are produced from the Rigaku MicroMax 007HF microfocus X-ray generator that is equipped with a Cu target. The X-ray dose rate was calibrated using a commercial dosimeter (451B Ionization Chamber Survey Meter, Fluke Biomedical).

2.6 Frequency domain thermoreflectance (FDTR) measurement

FDTR pump-probe technique (a well-established method) was adopted to determine the thermal conductivity and specific heat of (TEP)$InBr_4$ single crystals. To prepare the sample for FDTR measurement, a (TEP)$InBr_4$ crystal was first selected and coated with ~100 nm thick gold (Au) thin film. Thin film deposition process was achieved by using the Lesker Nano36 thermal evaporator (part of the Microfabrication Research & Education Center at the University of Oklahoma) to evaporate the gold pellet (purchased from Kurt J. Lesker Company, 99% purity). The deposited single crystal was then carefully placed on a glass substrate using double-sided carbon tape for FDTR measurement.

2.7 Computational methods

The computational studies were performed with DFT [18] as implemented in the SIESTA code [19, 20], with curated norm-conserving pseudopotentials obtained from the Pseudo-Dojo database [21]. We used the generalized gradient approximation by Perdew Burke Ernzerhof [22] for the exchange-correlation functional. The cutoff energy used for the atomic relaxations was 175 Ry, and we sampled the Brillouin zone (BZ) using a 6 × 6 × 6 Monkhorst-Pack grid [23]. The experimentally obtained crystal lattice parameters were used in the calculations. At the same time, the optimal atomic positions were found using the conjugate gradient method until all atomic force components were less

than 0.035 eV/Å. The electronic band structure and projected density of states (PDOS) calculations used the relaxed coordinates and a 12 × 12 × 12 Monkhorst-Pack grid for a finer sampling of the BZ. The PDOS calculation also made use of a Gaussian broadening of 0.1 eV.

3. Results and Discussion

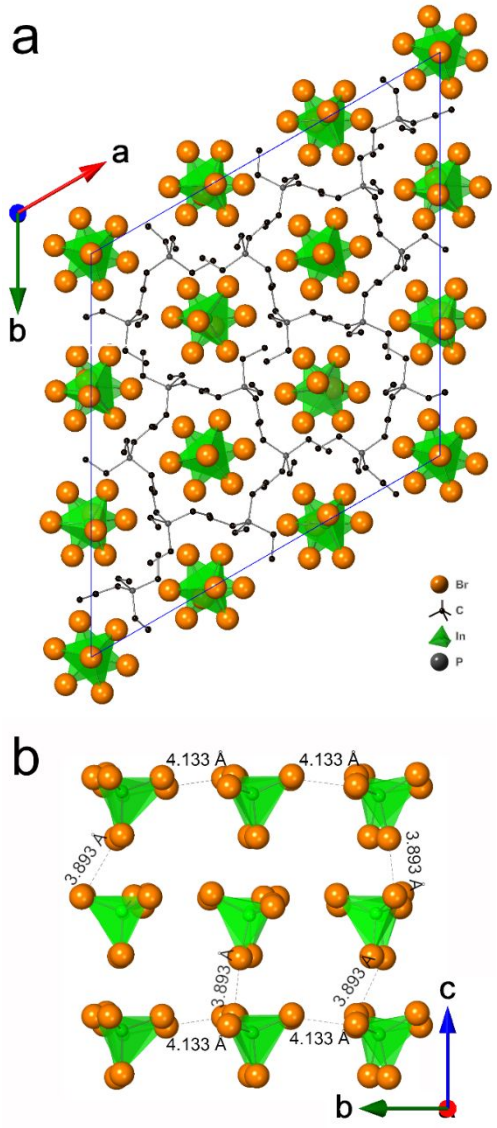

Figure 1. (a) Crystal structure of (TEP)$InBr_4$ viewed down the *c*-axis. Hydrogen atoms of the organic cation $C_8H_{20}P^+$ (TEP^+) are omitted for clarity. (TEP)$InBr_4$ contains isolated TEP^+ cations and tetrahedral $[InBr_4]^-$ anions in its 0D structure. (b) However, the $[InBr_4]^-$ anions are packed closely with inter-tetrahedra distances of ~4 Å.

(TEP)$InBr_4$ crystallizes in the hexagonal space group $P6_3$ (see Table 1). The 0D crystal structure of this compound contains molecular tetrahedral $[InBr_4]^-$ anions that are isolated by bulky organic TEP^+ cations (see Fig. 1). The $[InBr_4]^-$ tetrahedra show only a small distortion with the In – Br bond lengths

ranging from 2.498(2) Å to 2.508(5) Å and Br – In – Br bond angles ranging from 107.25(7) to 112.00(7)° (Table S2). Polyhedral distortions in metal halides are most typically attributed to electronic effects such as the presence of stereoactive ns^2 lone pair electrons, which does not apply in the case of In^{3+} with [Kr] $4d^{10}$ $5s^0$ electronic configuration. The observed bond lengths in $[InBr_4]^-$ are similar to that of the other indium bromides containing tetrahedral In^{3+} [24, 25] and are close to the sum of Shannon ionic radii for tetrahedral In^{3+} and Br^- ions, which is 2.58 Å [25]. Although (TEP)$InBr_4$ nominally has a 0D crystal structure, the separation between neighboring $[InBr_4]^-$ tetrahedra is small, the inter-tetrahedra Br – Br distances are 3.893 Å and 4.133 Å along the *c*- and *b*-axes, respectively (see Fig. 1b). These values are close to twice of the Shannon ionic radius for Br^-, which is 3.92 Å, and are comparable to the measured intra-tetrahedra (within $[InBr_4]^-$) Br-Br distance of 4.097 Å. Therefore, in contrast to the 0D crystal structure dimensionality of (TEP)$InBr_4$, its electronic structure may not be low-dimensional as band dispersion is expected due to the close packing of halide ions. This is reminiscent of the band dispersion observed for B-site deficient 0D perovskites A_2BX_6 [26, 27].

Table 1. Single crystal data and structure refinement parameters for (TEP)$InBr_4$.

Formula	**(TEP)$InBr_4$**
Formula weight (g/mol)	581.67
Temperature (K)	100(2)
Wavelength (Å)	0.71073
Crystal system	Hexagonal
Space group	$P6_3$
Z	18
Unit cell parameters	*a* = 25.5634(17) Å *b* = 25.5634(17) Å *c* = 13.7289(11) Å α = 90° β = 90° γ = 120°
Volume (Å^3)	7769.7(12)
Density (g/cm^3)	2.238
Absorption coefficient (μ) (mm^{-1})	10.690
θ_{min} - θ_{max} (°)	2.177 to 28.794
Reflections collected	103701
Independent reflections	13430
R^a indices ($I > 2\sigma(I)$)	R_1 = 0.0428 wR_2 = 0.1069
Goodness-of-fit on F^2	1.002
Largest diff. peak and hole (e$^-$/Å^3)	1.144 and -1.222

Our synthetic efforts suggest that (TEP)$InBr_4$ may be the only compound in the pseudo-binary TEPBr – $InBr_3$ system. The variations of reactant loading ratios did not yield any other products, unlike the related methylammonium bromide (MABr) and $InBr_3$ system [24]; in the case of the MABr – $InBr_3$

system, In^{3+} forms either tetrahedral $[InBr_4]^-$ as in $MAInBr_4$, octahedral $[InBr_6]^{3-}$ as in MA_4InBr_7 or both $[InBr_4]^-$ and $[InBr_6]^{3-}$ as is the case for MA_2InBr_5. In the present case, loading excess TEPBr does not lead to an increase in coordination number of In^{3+} from tetrahedral to octahedral, suggesting the structure-directing impact of the specific organic cation choice (e.g., H-bonding, steric influences, etc.) on the coordination environment preference of indium(III). Irrespective of the TEPBr:$InBr_3$ loading ratio, the utilized preparation method results in phase pure samples as confirmed by powder X-ray diffraction (PXRD) measurements (Figs. 2a and S1). Periodic PXRD measurements were further carried out over a period of two weeks to evaluate the stability of (TEP)$InBr_4$ in ambient air. Based on PXRD data, a slight decrease in peak intensities was recorded within days, indicating a crystallinity loss of (TEP)$InBr_4$ in ambient air (Fig. S2). In addition, thermal stability of (TEP)$InBr_4$ was assessed through simultaneous differential scanning calorimetry (DSC) and thermogravimetric analysis (TGA) measurements on (TEP)$InBr_4$ powder samples (Fig. 2b). The DSC heating curve shows two features at T=163.78 °C and T=236.15 °C. These two features are reversible as confirmed by the cooling cycle with the corresponding features at T=145.88 °C and T=224.41 °C, respectively. These results suggest that the features could either be congruent melting or structural phase transitions. A further melting point test using MEL-TEMP (Laboratory Devices Inc, USA) confirmed that (TEP)$InBr_4$ melts at 236.15 °C, while 163.78 °C is assigned to a structural transition. In addition to DSC-TGA, we further carried out frequency domain thermoreflectance measurements (Fig. S3). The measured FDTR data was fitted using a 2D diffusion thermal model to extract the thermal conductivity and specific heat values of (TEP)$InBr_4$. The thermal conductivity was determined to be between 0.33±0.05 and 0.45±0.07 W/(m-K), while the specific heat for (TEP)$InBr_4$ is between 682 and 909 J/(kg-K). The obtained low thermal conductivity here for (TEP)$InBr_4$ is consistent with the results for other low-dimensional metal halides, including 0.1 W/(m-K) for 2D $Rb_4Ag_2BiBr_9$ [28], 0.11 W/(m-K) for 2D hybrid perovskite $BA_2MA_3Pb_4I_{13}$ (BA=butylammonium) [29], and < 0.1 W/(m-K) for 0D $Cs_3Cu_2I_5$ [30]. Based on these results, potential practical applications of (TEP)$InBr_4$ would need addressing its air sensitivity (e.g., via encapsulation) and thermal characteristics (applications at around room temperature).

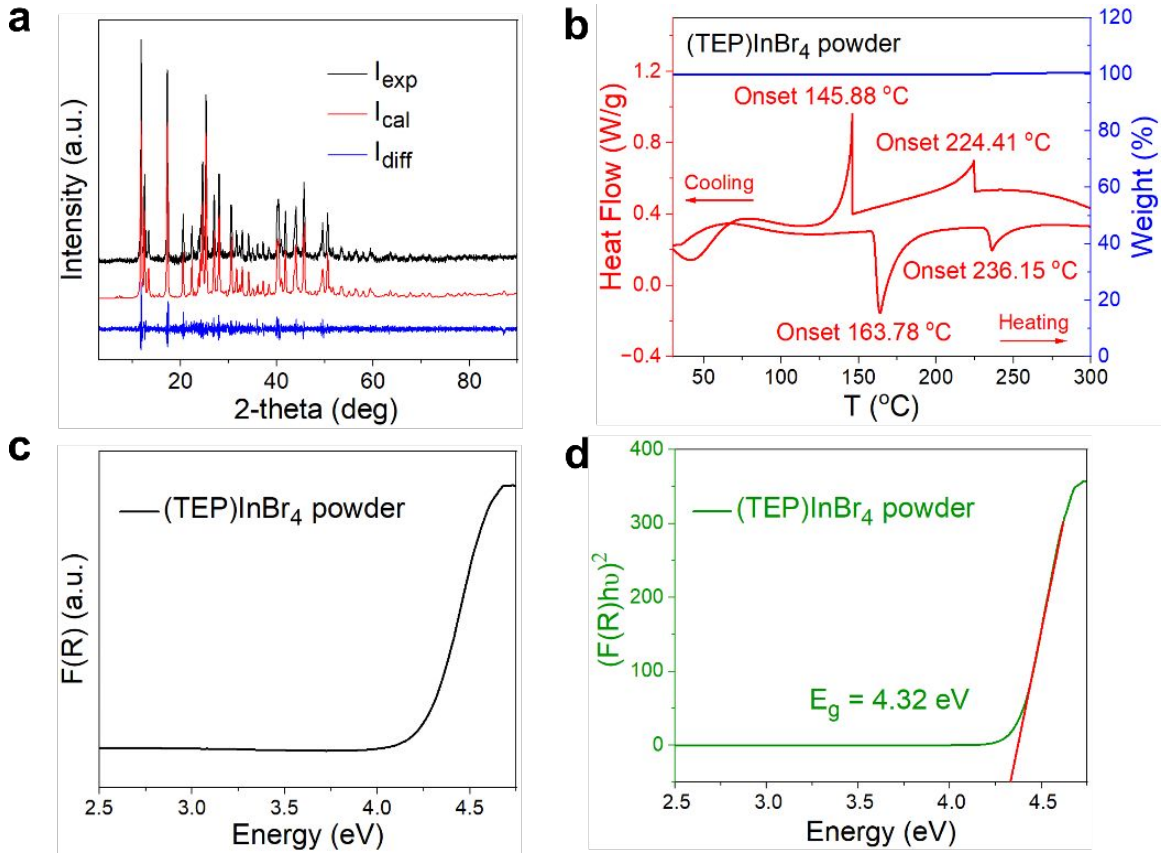

Figure 2. (a) The room temperature PXRD pattern (I_{exp}) for (TEP)$InBr_4$ fitted using the Pawley method (I_{cal}). (b) Simultaneous differential scanning calorimetry (DSC) and thermogravimetric analysis (TGA) measurement results for (TEP)$InBr_4$. (c) A pseudo-absorbance plot obtained using the diffuse reflectance data for a powdered (TEP)$InBr_4$ sample. (d) (TEP)$InBr_4$ has a large optical bandgap of 4.32 eV based on the fit of a Tauc plot assuming a direct bandgap.

To understand the optical and electronic properties of (TEP)$InBr_4$, we carried out diffuse reflectance and X-ray detection measurements using the as-grown (TEP)$InBr_4$ single crystals. Fig. 2c and 2d show the results of diffuse reflectance spectroscopy measurements. As expected for colorless crystals, (TEP)$InBr_4$ has a relatively large optical bandgap energy of 4.32 eV, which was obtained from a Tauc plot for a direct bandgap material. Moreover, to understand the potential of (TEP)$InBr_4$ for X-ray detection, we performed current-voltage (I-V) measurements to determine the semiconductor resistivity and the density of trap states in the as-grown (TEP)$InBr_4$ single crystals (see Fig. 3). For soft X-rays produced from an X-ray diffractometer (Cu target, E_{avg}=8 keV), the solution-grown 1 mm thick (TEP)$InBr_4$ single crystals are more than sufficient to achieve 100% photon attenuation (Fig. 3a). I-V measurement in Fig. 3b shows that (TEP)$InBr_4$ has a semiconductor resistivity of 1.72×10^{13} Ω·cm (also see Fig. S4 and Table S3 for the measured variation in resistivity from sample to sample), which is sufficiently high for reducing the detector leakage current to perform sensitive X-ray ionizing radiation detection. The density of trap levels in as-grown bulk (TEP)$InBr_4$ single crystals is measured using the space-charge-limited-current (SCLC) method (shown in Fig. 3c) and estimated using the formula below [31],

$$n_{trap} = \frac{2\varepsilon\varepsilon_0}{eL^2}V_{TFL}$$

where n_{trap} is the density of trap states, ε is the dielectric constant (= 9.56), ε_0 is the vacuum permittivity, e is the electronic charge, L is the crystal thickness, and V_{TFL} is the onset voltage of the trap-filled-limited (TFL) regime. The density of trap levels of as-grown (TEP)$InBr_4$ single crystals is determined to be 2.23×10^{11} cm^{-3}, which is comparable to that for 3D double perovskites $Cs_2AgBiBr_6$ (3.85×10^{10} cm^{-3}), 2D $Rb_4Ag_2BiBr_9$ (3.33×10^{10} cm^{-3}), and 1D $CsCu_2I_3$ (2.77×10^{11} cm^{-3}) [28, 32, 33]. In addition, for semiconductor radiation detector applications, the mobility-lifetime (mu-tau or $\mu\tau$) product serves as an important figure-of-merit. Here, we determined the mu-tau product in (TEP)$InBr_4$ single crystals according to the modified Hecht model or Many's equation below (Fig. 3d) [34],

$$I = \frac{I_0\mu\tau V\left(1-\exp\left(-\frac{L^2}{\mu\tau V}\right)\right)}{L^2\left(1+\frac{Ls}{V\mu}\right)}$$

where I is the X-ray induced photocurrent, I_0 is the saturated current, μ is the carrier mobility, τ is the carrier lifetime, L is again the crystal thickness (=0.1 cm), s is the surface recombination velocity, and V is the detector bias voltage. The determined mu-tau product is 2.07×10^{-5} cm^2/V, which is lower than that for 1D $CsPbI_3$ single crystals (3.63×10^{-3} cm^2/V) [35]; however, the obtained value is comparable to that of amorphous silicon (10^{-7} cm^2/V) [36] and thallium lead iodide (3.43×10^{-5} cm^2/V) [37] used for sensitive X-ray detection applications.

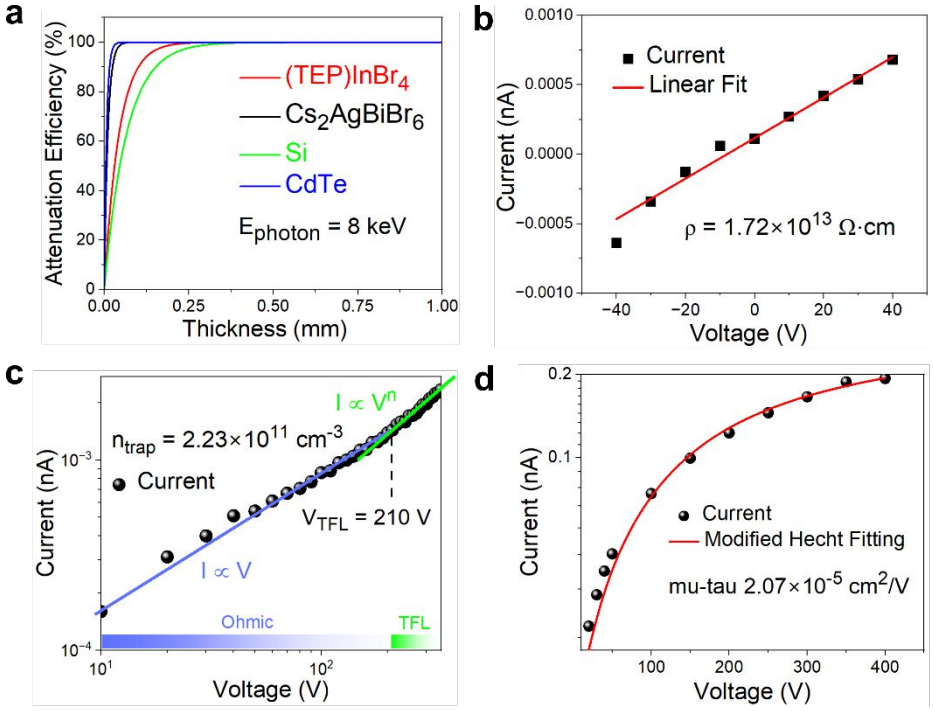

Figure 3. (a) Plot of the absorption efficiency vs. thickness for (TEP)$InBr_4$, 3D double perovskite $Cs_2AgBiBr_6$, silicon, and cadmium telluride (CdTe) under 8 keV soft X-rays to obtain the material thickness required for photon attenuation. (b) Current-voltage (I-V) measurement used to determine the semiconductor resistivity for (TEP)$InBr_4$ single crystals. (c) Space-charge-limited-current (SCLC) measurement for determining the defect trap levels in as-grown (TEP)$InBr_4$. (d) X-ray induced current measurements used to determine the mu-tau product using modified Hecht model.

Detector sensitivity and the lowest detectable dose rate are important figures of merit when evaluating the material's potential for sensitive X-ray radiation detection, especially in medical imaging applications. By fabricating a prototype X-ray detector using (TEP)$InBr_4$ single crystal, we demonstrated that 0D halide (TEP)$InBr_4$ is responsive to soft X-ray photons with a signal-to-noise (SNR) ratio of ~ 2860 at electric field E of 100 V/mm (see Fig. 4a, where SNR = $\frac{I_{x-ray\ on} - I_{x-ray\ off}}{I_{noise}}$), a rise and decay time of ~ 1.3 s (measured using 10% to 90% of the current amplitude, Fig. S5; note that the rise and decay time measured here include the time needed for turning the X-ray beam on and off). In addition, the fabricated prototype detector shows a detector sensitivity of 569.85 $uCGy^{-1}cm^{-2}$ at electric field E = 100 V/mm (see Fig. 4b), which is inferior compared to that for the 3D perovskite $MAPbI_3$ (1471.7 $uCGy^{-1}cm^{-2}$ at E =3.3 V/mm, [9]). This is expected, given the difference in the structural dimensionality and chemical contents of these two samples. However, despite its 0D structural dimensionality, (TEP)$InBr_4$ shows a relatively good detector performance that is comparable to the recently reported 2D halide $Rb_4Ag_2BiBr_9$, which has a detection sensitivity of 222.03 $uCGy^{-1}cm^{-2}$ at electric field E = 24 V/mm [28]. For (TEP)$InBr_4$, the detector sensitivity can be further enhanced if the detector is biased at higher voltages (see Fig. 4c and 4d). The determined lowest detectable dose rate is 38 nGy/s (see Fig. S6), which is much lower than the value required for X-ray diagnostic applications (2 R/h or equivalent 5.56 uGy/s) [38] and is even better than the reported 2D metal halide $BDAPbI_4$ [39]. The X-ray detector performance characteristics using 0D (TEP)$InBr_4$ single crystal is summarized in Table S4, compared to other reported metal halides. To further check the long-term detector operation stability under continuous X-ray irradiation, we exposed the prototype detector to X-rays generated from a tungsten X-ray tube (Fig. 4e). As expected, the X-ray induced current starts to drift down within the 10 minutes measurement period, which can be ascribed to the bromide halide ion migrations in the sample (a typical observation for thallium bromide (TlBr) and metal halide-based semiconductors) [40, 41].

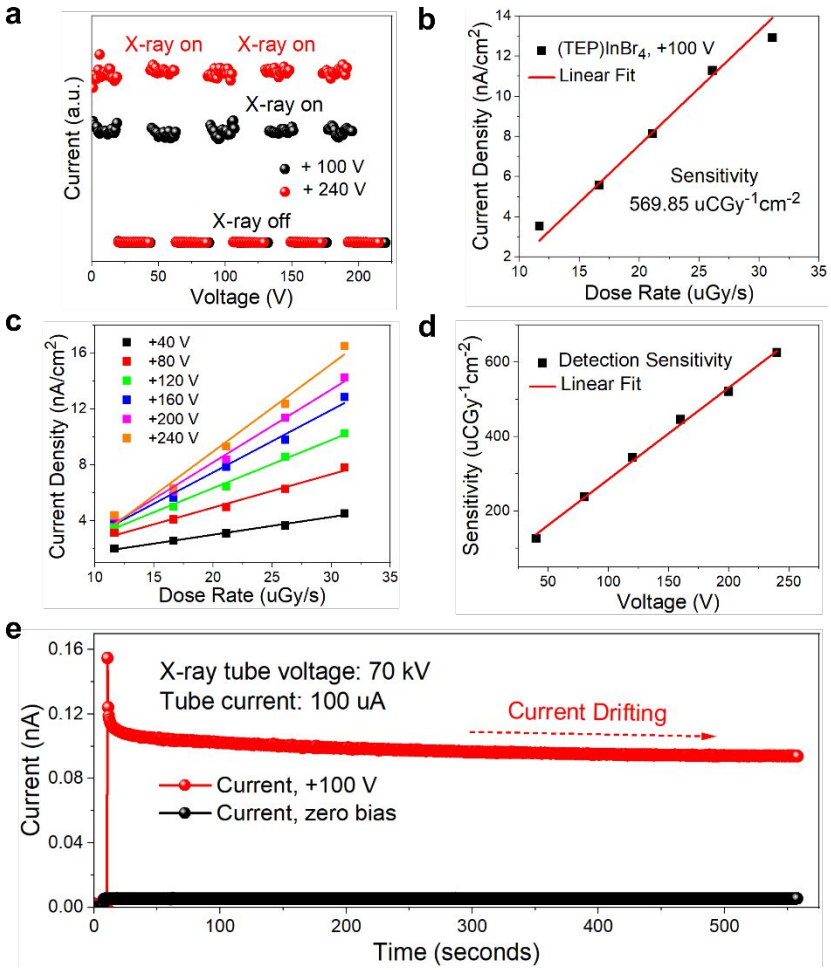

Figure 4. (a) X-ray on and off measurements used to demonstrate that (TEP)$InBr_4$ is highly responsive to low-energy soft X-ray photons; the measurement was performed at +100 V and +240 V, respectively. (b) Detector sensitivity measurement using (TEP)$InBr_4$ single crystals. (c-d) Detector sensitivity measurement and plot of the detection sensitivity obtained from +40 V to +240 V. (e) Detector operation stability testing over a period of 10 minutes under continuous Tungsten X-ray irradiation.

Finally, the electronic band structure and density of states (DOS) of (TEP)$InBr_4$ were calculated using DFT methods (Fig. 5). The compound exhibits a direct bandgap 3.485 eV at the Γ point (see Fig. 5a and Fig. S8 for a zoom-in plot), which is lower than the experimental bandgap estimated from diffuse reflectance data; the lower calculated gap energy is within expectations due to the tendency of DFT calculations to underestimate the bandgap. Fig. 5b shows the projected DOS results. As given by the PDOS plots, the highest occupied molecular orbitals (HOMOs) of (TEP)$InBr_4$ are dominated by the Br states, while the lowest unoccupied molecular orbitals (LUMOs) show contributions from both the Br and In states. The valence and conduction bands are dominated by the inorganic components, leading to relatively dispersive bands for a low-dimensional crystal structure. This observation is consistent with the close packing of the $[InBr_4]^-$ tetrahedra and the observation for other hybrid indium bromides using bulky organic cations such as $(C_4H_{14}N_2)_2In_2Br_{10}$ [42].

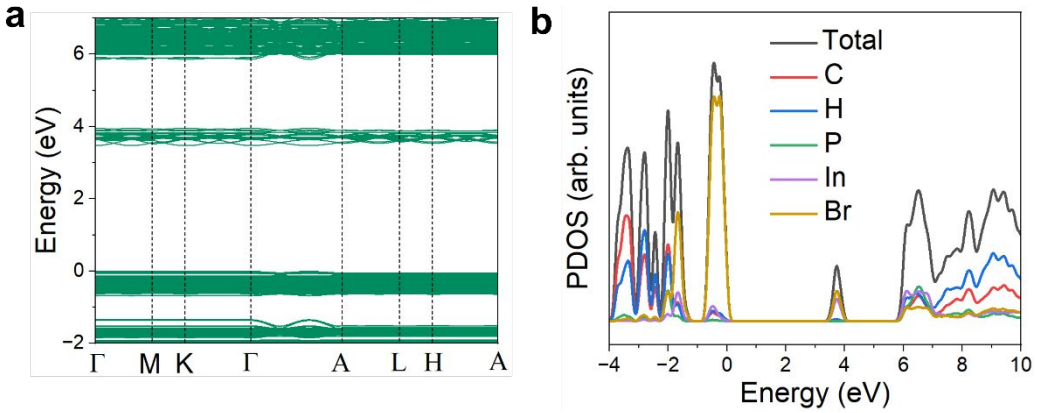

Figure 5. (a) Electronic band structure and (b) DOS plots of (TEP)$InBr_4$.

4. Conclusions

In summary, crystal growth, structural, optical, thermal, and electronic characterizations for the new 0D metal halide (TEP)$InBr_4$ are reported. Millimeter-sized (in length) colorless (TEP)$InBr_4$ single crystals can be readily prepared using the solution growth methodology. Computational DFT studies reveal that (TEP)$InBr_4$ is a direct bandgap semiconductor. The compound exhibits a thermal conductivity between 0.33±0.05 and 0.45±0.07 W/m-K with a bulk semiconductor single crystal resistivity of 1.72×10^{13} Ω·cm, and a mobility-lifetime (mu-tau) product of 2.07×10^{-5} cm^2/V. Moreover, the fabricated prototype X-ray detector based on (TEP)$InBr_4$ single crystals showed a detection sensitivity of 569.85 $uCGy^{-1}cm^{-2}$ (at electric field E = 100 V/mm) for soft X-ray photons of 8 keV. The results presented here demonstrated that 0D halide (TEP)$InBr_4$ could be a viable semiconductor material for soft X-ray radiation detection applications. More broadly, this work shows that novel metal halide semiconductors with nominally low-dimensional (0-2D) crystal structures can be incorporated into functioning radiation detectors.

Author Contributions

Zheng Zhang: conceptualization, formal analysis, investigation, validation, methodology, writing-original draft; Tony M. Pugliano: investigation, formal analysis; Da Cao: investigation, formal analysis; Doup Kim: investigation, formal analysis; Roshan S. Annam: investigation, formal analysis; Dilruba A. Popy: investigation; Tamanna Pinky: investigation; Ge Yang: supervision, writing-review & editing; Jivtesh Garg: supervision; Mario F. Borunda: investigation, formal analysis, writing-review & editing; Bayram Saparov: conceptualization, supervision, funding acquisition, writing-review & editing.

Conflicts of Interest

There are no conflicts to declare.

Acknowledgments

This material is based upon work supported by the U.S. Department of Energy, Office of Science, Office of Basic Energy Sciences, under the award number DE-SC0021158. We thank the chemical crystallography lab manager Douglas R. Powell at the Department of Chemistry & Biochemistry of the University of Oklahoma for his help with SCXRD measurements. X-ray response tests were conducted at the X-ray lab located at the Biomolecular Structure Core (BSC)-Norman, University of Oklahoma,

which is supported in part by an Institutional Development Award (IDeA) from the National Institute of General Medical Sciences of the National Institutes of Health (Award P20GM103640), the National Science Foundation (Award 0922269), and the University of Oklahoma Department of Chemistry and Biochemistry. We thank Dr. Leonard Thomas for his kind assistance with the X-ray measurements and Dr. Yingzhong Ma at the Oak Ridge National Laboratory for the constructive discussions and kind help with data analysis. Dr. Aaron Schmidt at Fourier Scientific LLC is also acknowledged for his kind help with thermal conductivity measurements.

References

1. Chen, J.; Tang, H.; Liu, B.; Zhu, Z.; Gu, M.; Zhang, Z.; Xu, Q.; Xu, J.; Zhou, L.; Chen, L.; Ouyang, X. High-Performance X-Ray Detector Based on Single-Crystal β-Ga2O3:Mg. *ACS Appl. Mater. Interfaces* **2021**, *13* (2), 2879–2886.
2. Roy, U. N.; Camarda, G. S.; Cui, Y.; Yang, G.; James, R. B. Impact of Selenium Addition to the Cadmium-Zinc-Telluride Matrix for Producing High Energy Resolution X-and Gamma-Ray Detectors. *Sci. Rep.* **2021**, *11* (1), 1–10.
3. Pipek, J.; Betušiak, M.; Belas, E.; Grill, R.; Praus, P.; Musiienko, A.; Pekarek, J.; Roy, U. N.; James, R. B. Charge Transport and Space-Charge Formation in Cd1-XZnxTe1-YSey Radiation Detectors. *Phys. Rev. Appl.* **2021**, *15* (5), 054058.
4. Bolotnikov, A. E.; Babalola, S.; Camarda, G. S.; Cui, Y.; Gul, R.; Egarievwe, S. U.; Fochuk, P. M.; Fuerstnau, M.; Horace, J.; Hossain, A.; Jones, F.; Kim, K. H.; Kopach, O. V.; McCall, B.; Marchini, L.; Raghothamachar, B.; Taggart, R.; Yang, G.; Xu, L.; James, R. B. Correlations between Crystal Defects and Performance of CdZnTe Detectors. *IEEE Trans. Nucl. Sci.* **2011**, *58* (4 PART 2), 1972–1980.
5. Ji, K.; Anaya, M.; Abfalterer, A.; Stranks, S. D. Halide Perovskite Light-Emitting Diode Technologies. *Adv. Opt. Mater.* **2021**, *9* (18), 2002128.
6. Muhammad, B. T.; Kar, S.; Stephen, M.; Leong, W. L. Halide Perovskite-Based Indoor Photovoltaics: Recent Development and Challenges. *Mater. Today Energy* **2022**, *23*, 100907.
7. Zhang, Z.; Saparov, B. Charge Carrier Mobility of Halide Perovskite Single Crystals for Ionizing Radiation Detection. *Appl. Phys. Lett.* **2021**, *119* (3), 30502.
8. Guo, J.; Wang, B.; Lu, D.; Wang, T.; Liu, T.; Wang, R.; Dong, X.; Zhou, T.; Zheng, N.; Fu, Q.; Xie, Z.; Wan, X.; Xing, G.; Chen, Y.; Liu, Y.; Guo, J.; Lu, D.; Wang, T.; Liu, T.; Wang, R.; Dong, X.; Zhou, T.; Fu, Q.; Wan, X.; Chen, Y.; Liu, Y.; Wang, B.; Xing, G.; Zheng, N.; Xie, Z. Ultra-Long Carrier Lifetime Exceeding 20 Ms in Lead Halide Perovskite Film Enable Efficient Solar Cells. *Adv. Mater.* **2023**, 2212126.
9. Geng, X.; Zhang, H.; Ren, J.; He, P.; Zhang, P.; Feng, Q.; Pan, K.; Dun, G.; Wang, F.; Zheng, X.; Tian, H.; Xie, D.; Yang, Y.; Ren, T. L. High-Performance Single Crystal CH3NH3PbI3 Perovskite X-Ray Detector. *Appl. Phys. Lett.* **2021**, *118* (6), 63506.
10. Jiang, W.; Ren, J.; Li, H.; Liu, D.; Yang, L.; Xiong, Y.; Zhao, Y. Improving the Performance and High-Field Stability of FAPbBr3 Single Crystals in X-Ray Detection with Chenodeoxycholic Acid Additive. *Small Methods* **2023**, *7* (4), 2201636.
11. Kunar, D. A.; Webster, M. F.; Wu, Y.; Kandel, R.; Wang, P. L. Development of Single Crystal CsPbBr3 Radiation Detectors from Low-Cost Solution Synthesized Material. *Crystals* **2023**, *13* (5), 762.

12. Pecunia, V.; Occhipinti, L. G.; Chakraborty, A.; Pan, Y.; Peng, Y. Lead-Free Halide Perovskite Photovoltaics: Challenges, Open Questions, and Opportunities. *APL Mater.* **2020**, *8* (10).
13. Ren, M.; Qian, X.; Chen, Y.; Wang, T.; Zhao, Y. Potential Lead Toxicity and Leakage Issues on Lead Halide Perovskite Photovoltaics. *J. Hazard. Mater.* **2022**, *426*, 127848.
14. Leão, C. R.; Lordi, V. Ionic Current and Polarization Effect in TlBr. *Phys. Rev. B - Condens. Matter Mater. Phys.* **2013**, *87* (8), 25–28.
15. Cho, J.; Dubose, J. T.; Le, A. N. T.; Kamat, P. V. Suppressed Halide Ion Migration in 2D Lead Halide Perovskites. *ACS Mater. Lett.* **2020**, *2* (6), 565–570.
16. Zheng, X.; Zhao, W.; Wang, P.; Tan, H.; Saidaminov, M. I.; Tie, S.; Chen, L.; Peng, Y.; Long, J.; Zhang, W. H. Ultrasensitive and Stable X-Ray Detection Using Zero-Dimensional Lead-Free Perovskites. *J. Energy Chem.* **2020**, *49*, 299–306.
17. Wang, Y.; Zhang, S.; Wang, Y.; Yan, J.; Yao, X.; Xu, M.; Lei, X. W.; Lin, G.; Yue, C. Y. 0D Triiodide Hybrid Halide Perovskite for X-Ray Detection. *Chem. Commun.* **2023**, 431–442.
18. Fiolhais, C.; Nogueira, F.; Marques, M. A Primer in Density Functional Theory. *Springer Science & Business Media* **2003**.
19. Soler, J. M.; Artacho, E.; Gale, J. D.; García, A.; Junquera, J.; Ordejón, P.; Sánchez-Portal, D. The SIESTA Method for Ab Initio Order-N Materials Simulation. *J. Phys. Condens. Matter* **2002**, *14* (11), 2745–2779.
20. García, A.; Papior, N.; Akhtar, A.; Artacho, E.; Blum, V.; Bosoni, E.; Brandimarte, P.; Brandbyge, M.; Cerdá, J. I.; Corsetti, F.; Cuadrado, R.; Dikan, V.; Ferrer, J.; Gale, J.; García-Fernández, P.; García-Suárez, V. M.; García, S.; Huhs, G.; Illera, S.; Korytár, R.; Koval, P.; Lebedeva, I.; Lin, L.; López-Tarifa, P.; Mayo, S. G.; Mohr, S.; Ordejón, P.; Postnikov, A.; Pouillon, Y.; Pruneda, M.; Robles, R.; Sánchez-Portal, D.; Soler, J. M.; Ullah, R.; Yu, V. W. Z.; Junquera, J. S Iesta: Recent Developments and Applications. *J. Chem. Phys.* **2020**, *152* (20), 204108.
21. Van Setten, M. J.; Giantomassi, M.; Bousquet, E.; Verstraete, M. J.; Hamann, D. R.; Gonze, X.; Rignanese, G. M. The PSEUDODOJO: Training and Grading a 85 Element Optimized Norm-Conserving Pseudopotential Table. *Comput. Phys. Commun.* **2018**, *226*, 39–54.
22. Perdew, J. P.; Burke, K.; Ernzerhof, M. Generalized Gradient Approximation Made Simple. *Phys. Rev. Lett.* **1996**, *77* (18), 3865–3868.
23. Monkhorst, H. J.; Pack, J. D. Special Points for Brillouin-Zone Integrations. *Phys. Rev. B* **1976**, *13* (12), 5188–5192.
24. Zhang, Z.; Fattal, H.; Creason, T. D.; Amiri, M.; Roseborough, A.; Gilley, I. W.; Nyman, M.; Saparov, B. Investigation of the Solution Chemistry of Hybrid Organic-Inorganic Indium Halides for New Material Discovery. *Inorg. Chem.* **2022**, *61* (33), 13015–13021.
25. Shannon, R. D. Revised Effective Ionic Radii and Systematic Studies of Interatomic Distances in Halides and Chalcogenides. *Acta Crystallogr., Sect. A: Cryst. Phys., Diffr., Theor. Gen. Crystallogr.* **1976**, *32*, 751– 767.
26. Saparov, B.; Sun, J. P.; Meng, W.; Xiao, Z.; Duan, H. S.; Gunawan, O.; Shin, D.; Hill, I. G.; Yan, Y.; Mitzi, D. B. Thin-Film Deposition and Characterization of a Sn-Deficient Perovskite Derivative Cs2SnI6. *Chem. Mater.* **2016**, *28* (7), 2315–2322.

27. Maughan, A. E.; Ganose, A. M.; Almaker, M. A.; Scanlon, D. O.; Neilson, J. R. Tolerance Factor and Cooperative Tilting Effects in Vacancy-Ordered Double Perovskite Halides. *Chem. Mater.* **2018**, *30* (11), 3909–3919.
28. Zhang, Z.; Ma, Y. Z.; Thomas, L.; Gofryk, K.; Saparov, B. Physical Properties of Candidate X-Ray Detector Material Rb4Ag2BiBr9. *Cryst. Growth Des.* **2022**, *22* (2), 1066–1072.
29. Giri, A.; Chen, A. Z.; Mattoni, A.; Aryana, K.; Zhang, D.; Hu, X.; Lee, S. H.; Choi, J. J.; Hopkins, P. E. Ultralow Thermal Conductivity of Two-Dimensional Metal Halide Perovskites. *Nano Lett.* **2020**, *20* (5), 3331–3337.
30. Jung, Y. K.; Han, I. T.; Kim, Y. C.; Walsh, A. Prediction of High Thermoelectric Performance in the Low-Dimensional Metal Halide Cs3Cu2I5. *npj Comput. Mater.* **2021**, *7* (1), 1–6.
31. Bube, R. H. Trap Density Determination by Space-Charge-Limited Currents. *J. Appl. Phys.* **1962**, *33* (5), 1733–1737.
32. Zhang, Z.; Cao, D.; Huang, Z.; Danilov, E. O.; Chung, C. C.; Sun, D.; Yang, G. Gamma-Ray Detection Using Bi-Poor Cs2AgBiBr6 Double Perovskite Single Crystals. *Adv. Opt. Mater.* **2021**, *9* (8), 2001575.
33. Han, S.; Quan, J.; Wang, D.; Li, H.; Liu, X.; Xu, J.; Zhang, Y.; Li, Z.; Wu, L.; Fang, X. Anisotropic Growth of Centimeter-Size CsCu2I3 Single Crystals with Ultra-Low Trap Density for Aspect-Ratio-Dependent Photodetectors. *Adv. Sci.* **2023**, *10* (7), 2206417.
34. Many, A. High-Field Effects in Photoconducting Cadmium Sulphide. *J. Phys. Chem. Solids* **1965**, *26* (3), 575–578.
35. Zhang, B. Bin; Liu, X.; Xiao, B.; Hafsia, A. Ben; Gao, K.; Xu, Y.; Zhou, J.; Chen, Y. High-Performance X-Ray Detection Based on One-Dimensional Inorganic Halide Perovskite CsPbI3. *J. Phys. Chem. Lett.* **2020**, *11* (2), 432–437.
36. Okamoto, H.; Kida, H.; Nonomura, S.; Fukumoto, K.; Hamakawa, Y. Mobility-Lifetime Product and Interface Property in Amorphous Silicon Solar Cells. *J. Appl. Phys.* **1983**, *54* (6), 3236–3243.
37. Hany, I.; Yang, G.; Phan, Q. V.; Kim, H. J. Thallium Lead Iodide (TlPbI3) Single Crystal Inorganic Perovskite: Electrical and Optical Characterization for Gamma Radiation Detection. *Mater. Sci. Semicond. Process.* **2021**, *121*, 105392.
38. Shearer, Douglas R.; Bopaiah, Mikhil. Dose Rate Limitations of Integrating Survey Meters for Diagnostic X-Ray Survevs. *Health Physics* **2000**, 79, S20-S21.
39. Shen, Y.; Liu, Y.; Ye, H.; Zheng, Y.; Wei, Q.; Xia, Y.; Chen, Y.; Zhao, K.; Huang, W.; Liu, S. Centimeter-Sized Single Crystal of Two-Dimensional Halide Perovskites Incorporating Straight-Chain Symmetric Diammonium Ion for X-Ray Detection. *Angew. Chemie - Int. Ed.* **2020**, *59* (35), 14896–14902.
40. Leão, C. R.; Lordi, V. Simultaneous Control of Ionic and Electronic Conductivity in Materials: Thallium Bromide Case Study. *Phys. Rev. Lett.* **2012**, *108* (24), 246604.
41. Zai, H.; Ma, Y.; Chen, Q.; Zhou, H. Ion Migration in Halide Perovskite Solar Cells: Mechanism, Characterization, Impact and Suppression. *J. Energy Chem.* **2021**, *63*, 528–549.
42. Zhou, L.; Liao, J. F.; Huang, Z. G.; Wei, J. H.; Wang, X. D.; Chen, H. Y.; Kuang, D. Bin. Intrinsic Self-Trapped Emission in 0D Lead-Free (C4H14N2)2In2Br10 Single Crystal. *Angew. Chemie - Int. Ed.* **2019**, *58* (43), 15435–15440.